Catalysis Science & Technology

ROYAL SOCIETY OF CHEMISTRY

PAPER

View Article Online
View Journal | View Issue

Cite this: *Catal. Sci. Technol.*, 2025, **15**, 5500

Facile synthesis of $SrNb_2O_6$ nanorods for enhanced selective conversion of fructose to 5-hydroxymethylfurfural

Peixin Wang,[a] Ruilong Zhang,[a] Ifunanya Rejoice Akaniro,[a] Puranjan Mishra,[a] Reeti Kumar[a] and Jun Zhao *[ab]

Catalytic dehydration of fructose to 5-hydroxymethylfurfural (HMF) is a key reaction in biomass valorization and sustainable chemistry. The development of solid acid catalysts with high selectivity for HMF remains challenging due to the formation of undesired by-products, such as levulinic acid and formic acid in the reaction. In this study, $SrNb_2O_6$ catalysts with various morphologies were prepared by a facile one-step hydrothermal method, triggering synergetic catalysis for selective transformation of fructose to HMF. Among the Nb-based mixed oxides synthesized under varying conditions, including different pH environments and Nb concentrations, $SrNb_2O_6$ nanorods (denoted as SNO-NR, with pH = 13 and Sr/Nb ratio of 1 : 2) demonstrated the highest catalytic performance. Specifically, it achieved a 74.9% HMF yield and a selectivity of 78.5% in DMSO at 120 °C for 1 hour. Comprehensive characterization analyses collectively indicated that an optimal acid capacity and a balanced Brønsted/Lewis acid ratio, which facilitate synergistic effects, are critical for achieving a highly selective conversion of fructose to HMF. Furthermore, it is also noteworthy that this SNO-NR catalyst was recyclable and stable for up to six runs with a minor reduction in its activity, confirming its remarkable robustness.

Received 22nd May 2025,
Accepted 25th July 2025

DOI: 10.1039/d5cy00613a

rsc.li/catalysis

1. Introduction

Increasing environmental concerns, including global warming and resource depletion resulting from the fossil fuel crisis, alongside the growing demand for sustainable development and the pursuit of low-carbon pathways, underscore the urgent need to expand the use of alternative and renewable energy sources.[1–3] Lignocellulose biomass, which is widely available and sustainable, can be expected to be a potential substitute for fossil fuels and industrial feedstock.[4] One of the key platform compounds that can be obtained from the conversion of biomass is 5-hydroxymethylfurfural (HMF) which offers a wide range of applications in petrochemical industries.[5,6] For instance, the oxidation of this furan-based chemical can produce 2,5-furandicarboxylic acid,[7] a polymer monomer for the production of packaging materials and bottle applications. Hydrogenolysis of HMF produces 2,5-dimethylfuran,[8] which is deemed as a potential biofuel with comparable energy density to conventional fossil fuels. Additionally, HMF could also be transformed into ethyl levulinate and liquid alkanes for various industrial applications.[9,10] HMF has been considered as the bridge between biomass-derived carbohydrates and the petroleum industry. Therefore, developing efficient synthetic methods for the production of HMF from carbohydrates has garnered growing interest.

Generally, HMF can be obtained through the conversion of mono-, di-, and polysaccharides under acidic conditions.[11,12] Among these available precursors, fructose is frequently selected for HMF synthesis owing to its preferred cyclic furanose form.[13,14] It is commonly employed as a model substrate in HMF production studies due to its high reactivity and well-understood conversion pathway, which facilitates the evaluation of new catalytic systems. This approach allows for detailed mechanistic analysis and benchmarking of catalyst performance. The main challenge in this reaction is the presence of side reactions leading to by-product formation and/or condensation of HMF to humins.[15] In this regard, the design of an efficient catalyst with enhanced selectivity to HMF is of great importance. A variety of homogeneous catalysts have been utilized for the dehydration of fructose to HMF, including mineral acids, organic acids, and ionic liquids.[16–18] However, these catalysts present several problems, such as equipment corrosion, difficulties in product separation, high costs, catalyst recovery issues, and lower product selectivity.[19] In contrast, solid acid catalysts are gaining increasing attention as valuable

[a] *Sino-Forest Applied Research Centre for Pearl River Delta Environment, Department of Biology, Hong Kong Baptist University, Hong Kong SAR. E-mail: zhaojun@hkbu.edu.hk*
[b] *Institute of Advanced Materials, Hong Kong Baptist University, Hong Kong SAR*

functional materials due to their enhanced acidity, environmentally friendly characteristics, and advantages such as easier separation, reduced corrosiveness, and improved safety. These attributes make them more desirable in the chemical industry compared to homogeneous acid catalysts.[20–22] Particularly, niobium oxide (Nb_2O_5) has emerged as a promising solid acid catalyst, demonstrating high acid strength and stable catalytic activity, and has been extensively applied in various reactions, including esterification, isomerization, hydrolysis, and dehydration.[23–25] Especially for the dehydration reaction, for example, Yang *et al.* reported the use of $Nb_2O_5{\cdot}nH_2O$ for this reaction in a water/2-butanol biphasic system at 160 °C for 50 min and obtained 89% HMF yield.[26] Complete conversion of fructose to HMF with an 86% yield was achieved using a home-synthesized Nb_2O_5 catalyst in DMSO at 400 °C by Wang *et al.*[19] However, it has been noticed that the use of bare Nb_2O_5 has several drawbacks such as poor reusability and extreme experimental conditions, which limits its potential application. Meanwhile the strategy of preparing mixed metal oxide catalysts appears to yield encouraging outcomes by improving acidic strength and enhancing the stability of these materials compared to pure Nb_2O_5 for various organic reactions.[27–29] For instance, a bifunctional Ta_2O_5/Nb_2O_5 nanocomposite providing both Lewis (24%) and Brønsted acid (76%) sites was employed in the systematic conversion of glucose into HMF, achieving 78.6% HMF and 86.5% selectivity after 3 h at 170 °C.[30] The highest selectivity to HMF was reported as *ca.* 80% by Garcia-Lopez *et al.* in the presence of 0.5 g L^{-1} Nb_2O_5–TiO_2 or Nb_2O_5–CeO_2 with a maximum fructose conversion of 70%.[31]

Among the various Nb-based mixed metal oxide catalysts, strontium niobate ($SrNb_2O_6$) is recognized for its advantageous physicochemical properties, suggesting its potential as an effective catalyst for the dehydration of fructose to 5-hydroxymethylfurfural (HMF). Its inherent acidic nature facilitates proton transfer reactions during the conversion process, while its distortable octahedral structure induces variations in the coordination environment of the active sites, enhancing selectivity. Additionally, its thermal stability ensures sustained catalytic activity at elevated temperatures, improving reusability.[32,33] Recently, $SrNb_2O_6$ nanostructures have been studied in photocatalytic organic dye degradation and H_2 production.[32,34] Ag-loaded $SrNb_2O_6$ and $Sr_2Nb_2O_7$ were also investigated for the photocatalytic reduction of CO_2 in H_2O where $SrNb_2O_6$ nanorods exhibited higher photocatalytic activity and selectivity toward CO evolution with amounts of CO (51.2 μmol h^{-1}) and H_2 (1.1 μmol h^{-1}) as the reduction products.[35] However, to the best of our knowledge, there are limited reports specifically exploring $SrNb_2O_6$ as a heterogeneous catalyst for fructose dehydration to HMF despite its potential. In addition, fabrication of the $SrNb_2O_6$ materials has been mostly restricted to conventional solid-state reactions, which typically require extensive mechanical mixing and high-temperature processing. This can result in significant particle agglomeration and a reduced surface area.[32] Meanwhile the hydrothermal synthesis, defined as a "bottom-up" soft chemical method, is expected to prepare $SrNb_2O_6$ catalysts due to its mild synthesis temperature, chemical homogeneity, high purity, and controlled size and morphology in comparison with the solid-state reaction, sol–gel method and other techniques.[36] Furthermore, it is recognized that monoclinic $SrNb_2O_6$ in crystalline structure was formed *via* a dissolution–crystallization mechanism. The amorphous $Nb_2O_5{\cdot}nH_2O$ can dissolve in an alkaline environment and produce $Nb_6O_{19}^{8-}$ or NbO_6^{7-} depending on the pH under hydrothermal conditions.[37] The pronounced pH dependence may provide insights into the role of Nb species in solution, influencing the morphology of the resulting product. The adjustment in the pH of the suspension to a higher value (pH = 13) was identified as crucial for achieving a morphology with desirable properties, regardless of the counter anion of Sr^{2+} or the reagent employed for pH adjustment.[34]

To this end, this study fabricated $SrNb_2O_6$ nanocrystalline catalysts under varied preparation conditions as depicted in Fig. 1 for efficient dehydration of fructose to HMF. Reaction parameters such as reaction temperature, catalyst dosage, and reaction time are optimized to improve the catalytic performance. Moreover, this work also investigates the reusability of the catalyst as well as the intrinsic mechanism/reaction pathway. The corresponding outcomes provide valuable insights into the development of Nb-based metal oxide catalysts for HMF production in the field of biomass conversion.

2. Materials and methods

2.1. Chemicals

All chemicals were acquired from commercial sources and used without further purification. Strontium nitrate ($Sr(NO_3)_2$, 99%, Thermo Scientific), strontium acetate ($Sr(Ac)_2$, 99%, Aladdin), strontium hydroxide ($Sr(OH)_2$, 95%, J&K), niobium oxide (Nb_2O_5, 99.9%, Aladdin), ammonium hydroxide ($NH_3{\cdot}H_2O$, 28.0–30.0%, Aladdin), nitric acid (HNO_3, 69%, VWR Chemicals), and sodium hydroxide (NaOH, 96%, Aladdin) were used for the synthesis of $SrNb_2O_6$ materials. Fructose (Bioreagent) and levulinic acid (LA, 98%) were obtained from Sigma Aldrich. Glucose (Bioreagent) and HMF (99%) were supplied by Shanghai Aladdin Biochemical Technology Co. Ltd. For the solvents use, both DMSO (dimethyl sulfoxide, ≥99.9%) and DMSO-d_6 (99.9% atom D) were also purchased from Shanghai Aladdin Biochemical Technology Co. Ltd.

2.2. Methods

2.2.1. Catalyst synthesis. In a typical procedure, for $SrNb_2O_6$ nanoparticles[34] (denoted as SNO-NP), 2 mmol of $Sr(NO_3)_2$ and 1 mmol of Nb_2O_5 precursor (Sr/Nb = 1 : 1) were added into 50 mL of distilled water under magnetic stirring. The pH of the suspension was adjusted to 8 by the addition of $NH_3{\cdot}OH$. Then the mixtures were sealed in a Teflon-lined stainless-steel autoclave and heated at 220 °C for 24 h. After cooling to room temperature, the obtained white product was washed with

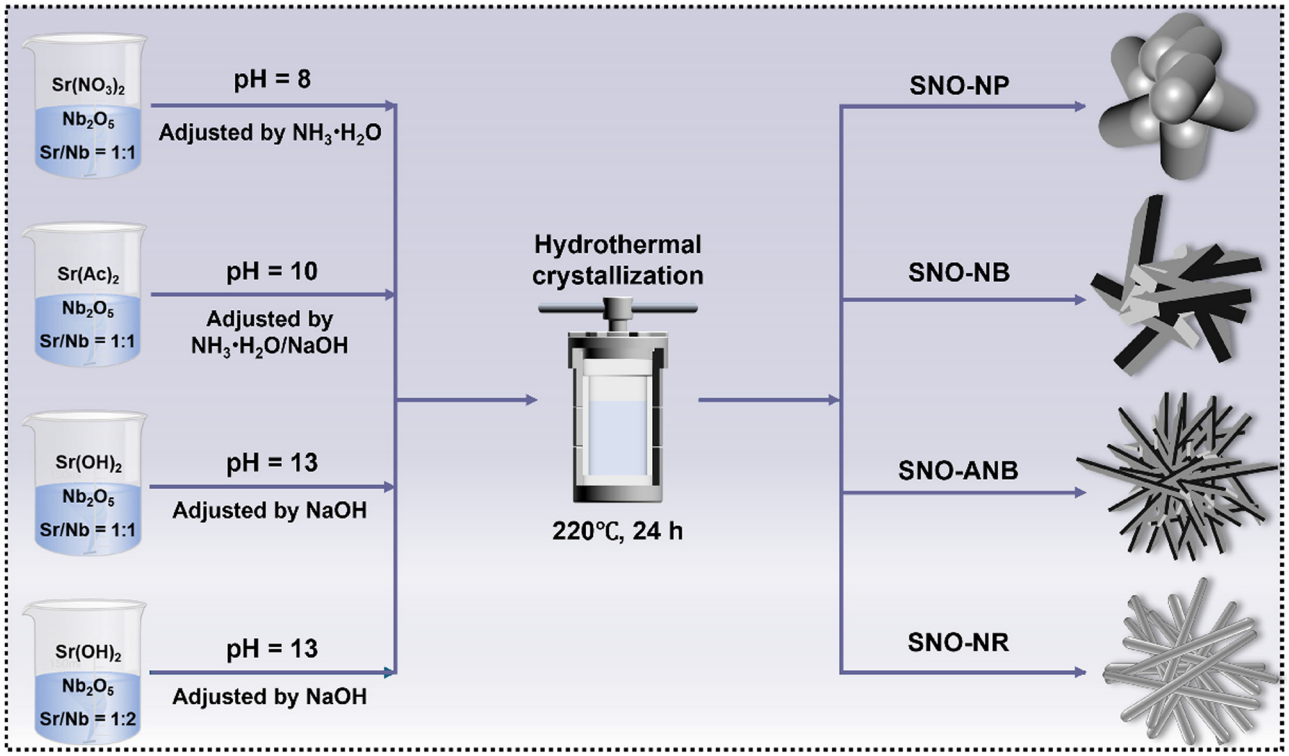

Fig. 1 Schematic illustration for the synthetic process of various $SrNb_2O_6$ nanocatalysts.

distilled water and 1 M HNO_3 (used when the added alkaline was $NH_3{\cdot}OH$) several times respectively and finally dried at 60 °C for 5 h. The synthesis process of $SrNb_2O_6$ nanobelts (denoted as SNO-NB) was similar to that of SNO-NP except that $Sr(Ac)_2$ was used as the precursor and the pH was adjusted to 10 by the addition of $NH_3{\cdot}OH$ or NaOH.[34,38] Likewise, the preparation of $SrNb_2O_6$ aggregated nanobelts (denoted as SNO-ANB) was also similar to that of SNO-NP except that $Sr(OH)_2$ was used as the precursor and the pH was adjusted to 13 by the addition of NaOH.[34] In addition, $SrNb_2O_6$ nanorods (denoted as SNO-NR) were prepared with identical synthesis to that of the SNO-ANB (Sr/Nb = 1 : 1) apart from the mole ratio of $Sr(OH)_2$ to Nb_2O_5 = 1 : 1 (Sr/Nb = 1 : 2).[34]

2.2.2. Catalyst characterization. The crystalline properties of all the catalysts were examined with powder X-ray diffraction (XRD, Rigaku Smartlab) with Cu Kα radiation (λ = 0.154 nm) as the incident beam, and all data were analyzed by MDI Jade 6.5 software. Fourier transform infrared spectra (FT-IR, PerkinElmer SPECTRUM 100) were used to reveal the surface functional groups existing in the catalysts in the scanning range of ~500–4000 cm^{-1}. The Brunauer–Emmett–Teller (BET) surface area and other pore characteristics of the catalysts were measured using a N_2 adsorption–desorption analyzer (Micromeritics ASAP 2460) after degassing under N_2 purging at 120 °C for 12 h. The surface morphologies of these nanomaterials were characterized by field emission scanning electron microscopy (FESEM, Zeiss Sigma 500). The structural morphologies and interplanar spacing of the nanomaterials were analyzed by using a transmission electron microscope coupled with an energy dispersive X-ray spectroscope (TEM-EDX, FEI Tecnai G2 F20 S-TWIN) operating at 200 kV. X-ray photoelectron spectroscopy (XPS, Thermo K-Alpha+) was performed to detect the chemical states of the surface elements using a VG Escalab 250 EPS instrument equipped with a high-intensity monochromated Al Kα source focused to a spot 400 μm in diameter on the sample and all data were analyzed by Avantage software. To characterize the stability of acid sites on the samples at elevated temperatures, Fourier transformed infrared (FT-IR) spectra of adsorbed pyridine (Py-FTIR, Bruker Tensor 27) were obtained stepwise by desorbing the adsorbed pyridine at different temperatures. Details of its procedures and the calculation method for acid amounts are shown in Text S1.

2.2.3. Catalytic dehydration experiments. In a representative dehydration reaction, a 4 wt% fructose solution (5 mL DMSO) was added into a 25 mL three-necked round bottom flask containing 0.05 g catalyst. Constant temperature heating magnetic stirrers (MS-H380-Pro, DLAB) filled with silicone oil were used to conduct the conversion of fructose into HMF at predetermined conditions of 110 °C for 1 h. After reaction, the obtained mixtures were centrifuged at 5000 rpm for 3 min. Then the supernatants were filtered through a 0.22 μm pore-size membrane filter prior to high-performance liquid chromatography (HPLC, Agilent, Germany) analysis for further quantification. Control experiments without catalysts were also conducted while all other conditions were kept consistent. The effects of reaction

temperature, catalyst dosage, and reaction time on the dehydration efficiency of fructose into HMF over SNO were also investigated. As for reusability tests of SNO catalysts, they were usually recycled by centrifugation after reaction, then washed twice with ethanol, and oven-dried at 60 °C for future reuse. The recyclability of the reactivated catalysts was evaluated with consecutive reaction runs under the same reaction conditions.

2.2.4. Product analysis. In order to determine the degree of fructose conversion and HMF yield, all obtained products were analyzed using an HPLC equipped with a Bio-Rad Aminex HPX-87H column (300 × 7.8 mm) maintained at 60 °C with a 0.6 mL min^{-1} flow rate of 5 mM H_2SO_4 as the mobile phase. Fructose conversion (eqn (1)), HMF yield (eqn (2)), and HMF selectivity (eqn (3)) were calculated as follows.

$$\text{Fructose conversion, } C = \left(1 - \frac{\text{final mole of fructose}}{\text{initial mole of fructose}}\right) \times 100 \quad (1)$$

$$\text{HMF yield, } Y = \frac{\text{produced mole of HMF}}{\text{initial mole of fructose}} \times 100 \quad (2)$$

$$\text{HMF selectivity, } S = \frac{\text{produced mole of HMF}}{\text{converted mole of fructose}} \times 100 \quad (3)$$

Gas chromatography-mass spectrometry (GC-MS, Agilent-7890A for the GC system and Agilent-5975C for the MS system with a Triple-Axis Detector) was employed to identify the types of by-products. Liquid phase ^1H nuclear magnetic resonance (NMR) spectra were obtained with a Bruker Ascend-400 spectrometer (400 MHz), investigating the pathway of fructose conversion to HMF over the target catalyst. Details of its procedures can be found in Text S2.

3. Results and discussion

3.1. Catalyst characterization

3.1.1. Structural studies and morphological characterization. The schematic illustration for the fabrication of $SrNb_2O_6$ nanomaterials (denoted as SNO) with different morphologies is shown in Fig. 1 where a facile hydrothermal method was applied. According to the diverse morphologies obtained based on different strontium precursors and pH conditions, the as-prepared catalysts were labeled as SNO-NP ($SrNb_2O_6$ nanoparticles), SNO-NB ($SrNb_2O_6$ nanobelts), SNO-ANB ($SrNb_2O_6$ aggregated nanobelts), and SNO-NR ($SrNb_2O_6$ nanorods), respectively. Fig. 2a shows the XRD patterns of the as-prepared SNO catalysts under different synthesis conditions. As observed in the figure, the diffraction peaks in all the catalysts at approximately 22.6°, 23.1°, 28.4°, 29.2°, 32.1°, 36.7°, 40.2°, 43.3°, 46.3°, 47.1°, 55.3°, and 56.4° match well with the (012), (200), (202), (013),

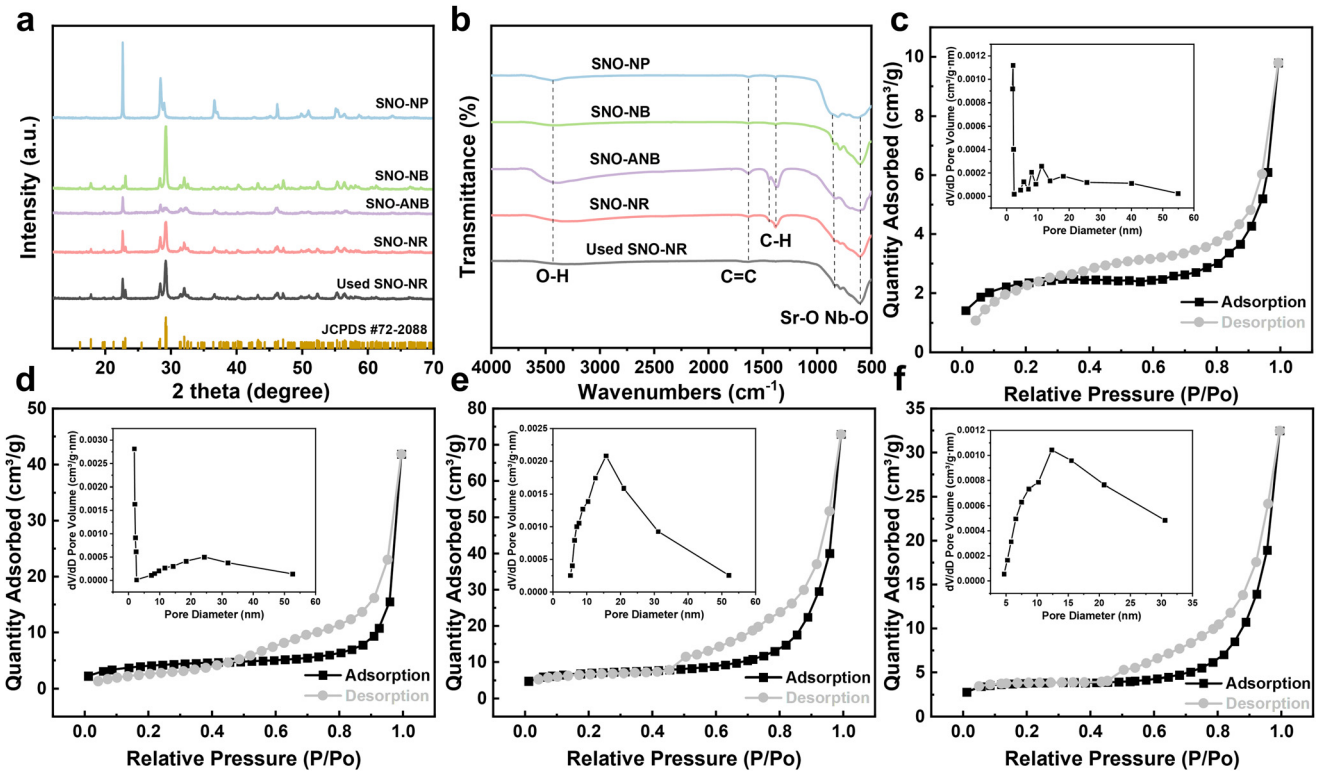

Fig. 2 (a) XRD patterns and (b) FT-IR profiles of all the SNO catalysts including the spent SNO-NR. The N_2 adsorption–desorption isotherms of (c) SNO-NP, (d) SNO-NB, (e) SNO-ANB, and (f) SNO-NR, respectively.

(020), (014), (204), (222), (024), (400), (033), and (413) lattice planes of monoclinic $SrNb_2O_6$ (JCPDS card, No. 72-2088).[32] The XRD result suggested the successful synthesis of highly crystalline $SrNb_2O_6$. Moreover, the crystallinity of the SNO-NR catalysts after reuse remained largely unaffected, suggesting its stability. It was revealed that variations in synthesis conditions between SNO-NP, SNO-NB, SNO-ANB, and SNO-NR could lead to different growth kinetics and crystallographic orientations, presenting various crystal sizes along with different prominent crystal faces but the bulk structure still exhibited the crystal characteristics of $SrNb_2O_6$. For example, the peaks of SNO-NP were the sharpest whereas SNO-ANB featured the broadest peaks, which could probably be associated with their crystal sizes. Large crystal sizes lead to sharp peaks while small crystal sizes result in peak broadening. Additionally, certain planes may diffract more strongly if the sample has a preferred orientation or texture, resulting in higher peak intensities for specific reflections.[39–41] This could possibly account for the most prominent peak of SNO-NP at 23.1° instead of 29.2° which was more applicable for other materials. Surface functional groups of these SNO catalysts were further identified by FT-IR spectroscopy as seen in Fig. 2b. The distinct bands at ~3435 cm^{-1}, 1635 cm^{-1}, 1380 cm^{-1}, and 835–606 cm^{-1} are assigned to the O–H, C═C, C–H, and Sr–O/Nb–O stretching vibrations, respectively.[42–44] It could be observed that the metal-oxide stretching vibrations of SNO-NP were more prominent and intense than those of the other SNO catalysts. This may be associated with its larger crystal size leading to improved crystallinity and reduced scattering effects, which was consistent with the XRD results. Moreover, in the profiles of SNO-ANB and SNO-NR, the relatively more pronounced peaks of O–H, C═C, and C–H vibrations might result from different pH environments during the synthesis process. The availability of hydroxide ions under more basic conditions could promote the adsorption of water molecules and carbon-containing species, facilitating the formation of surface functional groups including O–H, C═C, and C–H bonds on the catalyst surface. The presence of these carbon-containing species could enhance the affinity for organic substrates, facilitating their adsorption and subsequent transformation during catalytic reactions. They may thus potentially result in improved catalytic performance. Nevertheless, the intensity of the C–H band noticeably disappeared when the spent SNO-NR was subject to subsequent recovery possibly owing to the decomposition of carbonaceous species at elevated reaction temperatures or their elimination during washing procedures. It is also worth mentioning that the fainter presence of O–H groups in SNO-NR may be attributed to a higher Nb addition compared to that in SNO-ANB, leading to a more Brønsted acidic environment facilitating the interaction with hydroxyl groups.[45,46] Their textural properties summarized in Table 1 were characterized by N_2 adsorption–desorption measurements with their isotherms demonstrated in Fig. 2c–f as well. As shown in the table, SNO-NP exhibited the lowest surface area (8.42 $m^2\ g^{-1}$) along with the smallest pore diameter (7.20 nm) and pore volume (0.02 $cm^3\ g^{-1}$) when compared with the other SNO catalysts. This may be attributed to the effects of faster precipitation kinetics and agglomeration under mildly acidic conditions. Faster crystallization under lower pH values may lead to larger crystal sizes and reduced surface area due to the limited nucleation and growth of smaller particles with higher surface-to-volume ratios,[47] which in turn affected the catalytic performance. By contrast, SNO-NB, SNO-ANB, and SNO-NR possessed higher surface areas, increased pore volumes, and larger pore diameters ranging from 14.00–25.51 $m^2\ g^{-1}$, 0.05–0.11 $cm^3\ g^{-1}$, and 13.73–18.50 nm, respectively. This could be ascribed to improved dispersion, reduced agglomeration, and enhanced porosity under a more basic environment. Among them, SNO-ANB with a smaller ratio of Nb addition compared to SNO-NR featured an extraordinarily highest surface area of 25.51 $m^2\ g^{-1}$, which may be primarily associated with the growth rates of certain crystal facets or phases leading to the formation of void spaces and interparticle boundaries.[48,49] This could account for its propensity for potentially enhanced catalytic activity. Fig. 2c–f and Fig. S1 display type IV isotherms for all the SNO catalysts, indicating the existence of typical mesoporous structures in them. In addition, the porosity properties of SNO-NR after reuse remained almost unchanged and even slightly improved from both Table 1 and Fig. S1, indicating the conspicuous reusability of SNO-NR which was in accordance with the aforementioned discussion. It could be concluded that the crystallization behaviors during the synthesis process under different pH conditions influenced not only the porosity properties of these $SrNb_2O_6$ catalysts, but also the crystal growth orientations as well as morphologies.

The above conclusion could be further supported by the FESEM and TEM images (Fig. 3), from which both surface and structural morphologies of SNO catalysts were revealed.

Table 1 The textural properties of various $SrNb_2O_6$ catalysts

Entry	Catalysts	Surface area ($m^2\ g^{-1}$) S_{BET}	Pore volume ($cm^3\ g^{-1}$) Total pore	Average pore diameter (nm)
1	SNO-NP	8.42	0.02	7.20
2	SNO-NB	14.00	0.06	18.50
3	SNO-ANB	25.51	0.11	17.68
4	SNO-NR	14.63	0.05	13.73
5	Used SNO-NR	15.29	0.08	20.77

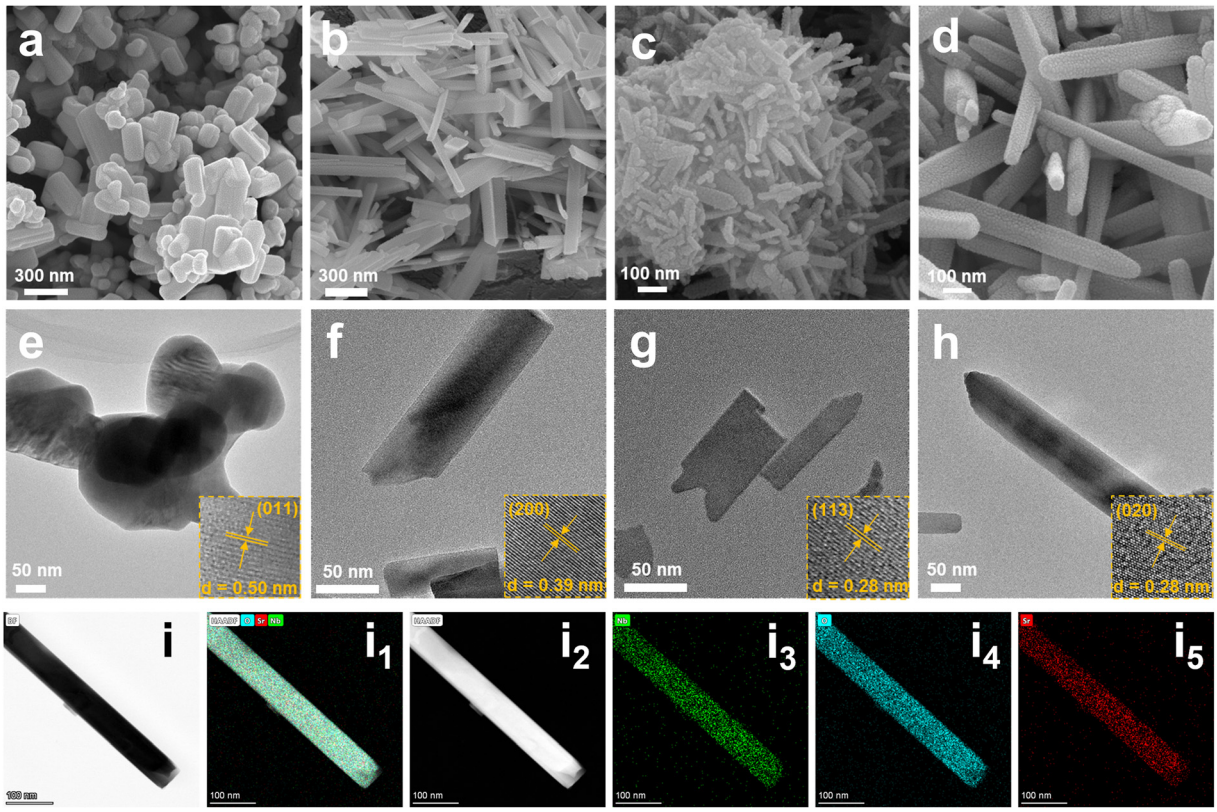

Fig. 3 FESEM images of (a) SNO-NP, (b) SNO-NB, (c) SNO-ANB, and (d) SNO-NR, respectively. (e–h) TEM images of these SNO nanomaterials accordingly as well as their magnification. (i–i5) TEM mapping images of SNO-NR.

It can be seen from Fig. 3a–d that these SNO nanomaterials exhibited diverse morphologies including nanoparticles, nanobelts, and nanorods, different from the reported morphologies by Xie *et al.*[34] such as plate-like shapes. It is important to note that while our synthesis approach was largely guided by established methods, the differences in material sources and equipment resulted in unique catalysts with distinct properties. This underscores the importance of synthesis conditions in tailoring catalyst characteristics. Specifically, SNO-NP (Fig. 3a) featured rod-like nanoparticles which aggregated together. Fig. 3b (SNO-NB) shows bundled and intersected nanobelts. Irregular aggregation consisting of nanobelt composites in different sizes is found in Fig. 3c (SNO-ANB) with smaller thicknesses and higher-degree interpenetration. Comparatively, more regular and uniform nanorod morphologies appeared in SNO-NR as seen from Fig. 3d. These described morphologies were basically consistent with the TEM micrographs (Fig. 3e–h), where various clear lattice fringes were involved with an interlayer spacing of 0.50 nm, 0.39 nm, 0.28 nm, and 0.28 nm ascribed to the (011), (200), (113), and (020) lattice plane of $SrNb_2O_6$, respectively. Furthermore, TEM mapping results in Fig. 3i manifested the uniform distribution of these elements on the catalyst surface, indicating the successful synthesis of $SrNb_2O_6$ nanostructure. Collectively, the related parameters of crystal growth sizes corresponding to these four morphologies are summarized in Table 2. As shown in the table, both the length and diameter/width of SNO-NP and SNO-NR (300–400 nm and 80–140 nm, respectively) appeared to be larger than those of the other two SNO catalysts (100–179 nm and 20–52 nm, respectively). The large crystal size of SNO-NP along both two dimensions produced the lowest aspect ratio of 2.14, possibly resulting from the effects of faster crystallization and poor nucleation under a lower pH environment. Meanwhile SNO-ANB and SNO-NR featured the highest aspect ratio of 5.00 which may be attributed to the promoted anisotropic growth and favorable elongation along a particular crystallographic direction under a more

Table 2 Summary of related parameters of various $SrNb_2O_6$ catalysts

Catalysts	Precursor	Sr/Nb ratio	pH	Morphology	Length (nm)	Diameter/width (nm)	Aspect ratio
SNO-NP	$Sr(NO_3)_2 + Nb_2O_5$	1 : 1	8	Rod-like nanoparticles	~300	~140	2.14
SNO-NB	$Sr(Ac)_2 + Nb_2O_5$	1 : 1	10	Nanobelts	~179	~52	3.44
SNO-ANB	$Sr(OH)_2 + Nb_2O_5$	1 : 1	13	Aggregated nanobelts	~100	~20	5.00
SNO-NR	$Sr(OH)_2 + Nb_2O_5$	1 : 2	13	Nanorods	~400	~80	5.00

alkaline environment. This could aptly account for their corresponding order in the surface area as shown in Table 1, where SNO-NP exhibited the lowest surface area due to its large crystal size and minimum aspect ratio. Meanwhile the highest surface area was observed in SNO-ANB resulting from its smallest crystal size as well as highest aspect ratio. As for SNO-NR, the same high aspect ratio compensated for the effects of the largest crystal size along one dimension, leading to its halfway value in terms of surface area. Likewise, a similar tendency could be observed in the XRD peaks, where peak broadening existed in the case of SNO-ANB due to its smallest crystal size, whereas SNO-NP exhibited the sharpest peaks compared to others resulting from its large crystallite size along both two dimensions. These results were in good alignment with the aforementioned discussion.

3.1.2. Acid properties and XPS analysis. Considering that the type and quantity of acid sites on the catalyst surface could play a pivotal role in the selective dehydration of fructose to HMF, FT-IR experiments on pyridine adsorption at 150 °C were afterwards carried out to identify and quantify Brønsted acid and Lewis acid sites on the SNO catalysts. Fig. 4a shows the Py-FTIR spectra of these catalysts. There are mainly three distinguished pyridine FT-IR peaks within the range of 1400–1600 cm^{-1}. Specifically, the characteristic adsorption peaks at 1444 cm^{-1} could be assigned to the Lewis acid sites (denoted as L). The peaks at 1490 cm^{-1} could be attributed to the overlap of the Brønsted and Lewis acid sites (denoted as L + B). Besides, the peaks at 1540 cm^{-1} could be ascribed to the Brønsted acid sites (denoted as B).[50] It is well acknowledged that B-acid sites facilitate the protonation of fructose, promoting its dehydration to generate HMF. Meanwhile L-acid sites can not only help in activating fructose through coordination but also stabilizing the transition states or intermediates formed during the reaction.[51–55] The synergistic effect between L and B acid sites could give rise to the remarkable catalytic efficiency of these as-synthesized catalysts. It could also be observed from Fig. 4a that the peak intensity of these acid sites in the spectra of SNO-ANB and SNO-NR was more pronounced than that of SNO-NP and SNO-NB. Fig. 4b further illustrates the comparison between the amounts of these acid sites on the catalyst surface more clearly and intuitively with their related acid parameters summarized in Table 3 as well. As shown in the figure, SNO-NR featured the highest amounts of L and B acid sites with 78.48 and 42.12 μmol g^{-1}, respectively, while the lowest acid amounts were found in SNO-NP with only 6.89 μmol g^{-1} of L acid and 0.61 μmol g^{-1} of B acid. Similar to the trend observed in Fig. 4a, the acid amounts in the latter two SNO catalysts were far higher than the former two catalysts. This result could largely account for enhanced catalytic performance of SNO-ANB and SNO-NR as more active sites corresponding to their higher acid density could be available for the reaction. After reaction, the total acid

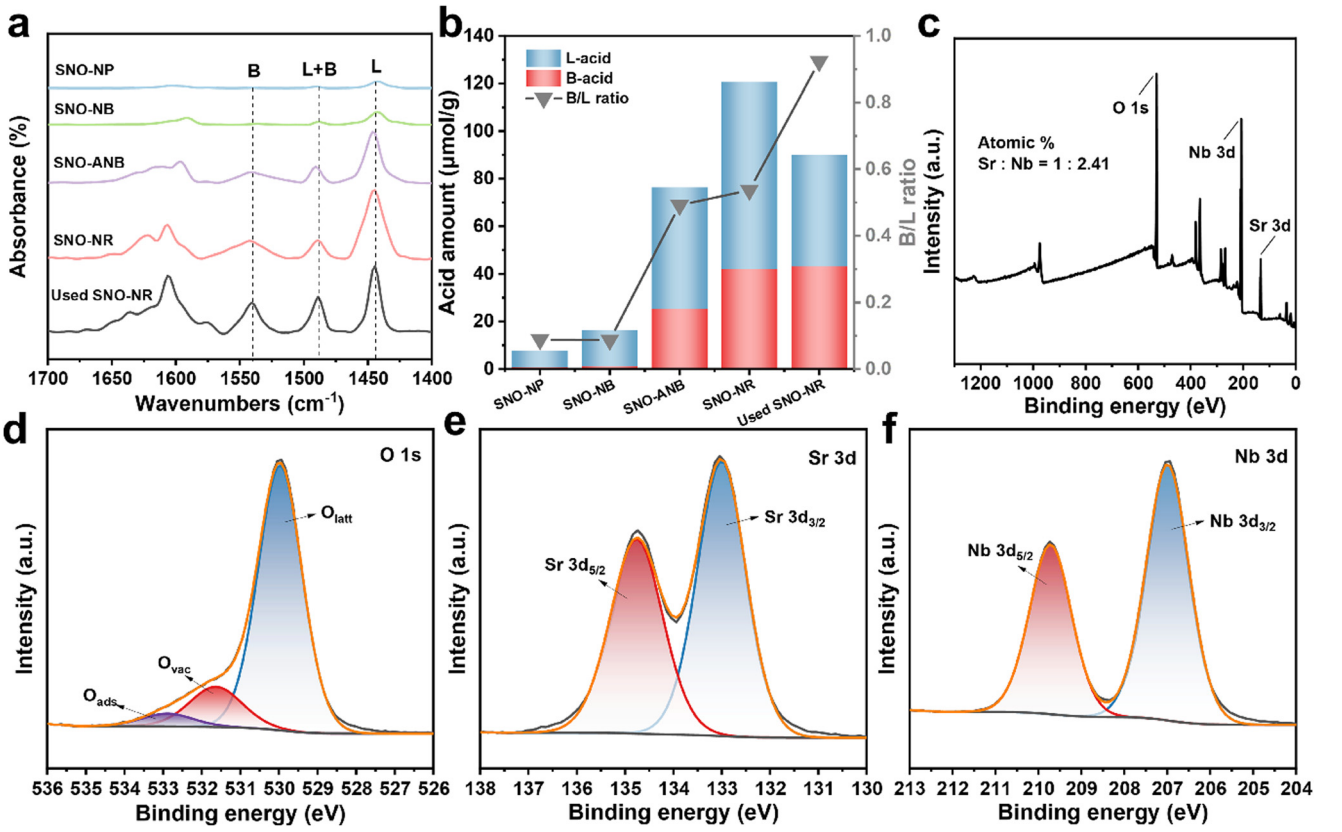

Fig. 4 (a) Pyridine-desorption FT-IR spectra at 150 °C and (b) acid properties of all the SNO catalysts including the spent SNO-NR. XPS spectra of the SNO-NR catalyst: (c) survey spectrum, (d) O 1s spectrum, (e) Sr 3d spectrum, and (f) Nb 3d spectrum, respectively.

Table 3 The acid amounts of various $SrNb_2O_6$ catalysts

Entry	Catalysts	Acid amount (μmol g^{-1})			B/L ratio
		B acid	L acid	Total	
1	SNO-NP	0.61	6.89	7.50	0.09
2	SNO-NB	1.31	15.03	16.34	0.09
3	SNO-ANB	25.13	51.12	76.24	0.49
4	SNO-NR	42.12	78.48	120.60	0.54
5	Used SNO-NR	43.18	46.77	89.94	0.92

density of SNO-NR decreased from the original 120.60 μmol g^{-1} to 89.94 μmol g^{-1} with L acid declining to 46.77 μmol g^{-1} and B acid almost unchanged. This may lead to decreased catalytic activity and selectivity of SNO-NR after reuse. The slight decline of acid density for the used SNO-NR also confirmed its robustness which aligned with the discussion in section 3.1.1. In terms of the B/L ratio, SNO-NP and SNO-NB exhibited the lowest value (0.09), whereas the spent SNO-NR demonstrated the highest (0.92). This indicated that an optimal ratio between L and B acid sites is crucial. A high B/L ratio could enhance the protonation and dehydration steps leading to higher HMF yield. However, imbalances such as too high B/L ratio may result in increased formation of undesired byproducts and thus decreased catalytic efficiency.[56,57]

The XPS spectra displayed in Fig. 4c–f demonstrate the chemical states and surface composition of the SNO-NR catalyst. The XPS survey (Fig. 4c) shows the typical peaks of O 1s, Nb 3d, and Sr 3d. Besides, the atomic ratio of metallic element Sr to Nb was close to 1 : 2, further proving the successful synthesis of $SrNb_2O_6$. The O 1s spectra shown in Fig. 4d were deconvoluted into three dominant peaks at ~529.9 eV, 531.6 eV, and 532.8 eV, attributed to lattice oxygen in the metal–oxygen bond (O_{latt}), surface oxygen vacancies (O_{vac}), and chemically adsorbed hydroxide species due to moisture or contamination (O_{ads}), respectively.[58] In the Sr 3d spectra (Fig. 4e), two dominant peaks centered at ~133.0 eV and 134.7 eV were observed after deconvolution, which were assigned to Sr $3d_{3/2}$ and Sr $3d_{5/2}$, respectively. They were both associated with Sr^{2+} ions present in oxide compounds containing Sr–O bonds.[59,60] Moreover, the Nb 3d spectra shown in Fig. 4f involve two splits of Nb $3d_{3/2}$ and Nb $3d_{5/2}$, where deconvoluted peaks centered at ~207.0 eV and 209.7 eV were both ascribed to the presence of Nb^{5+} ions regarding Nb–O bonds.[61,62]

3.2. Catalyst activity evaluation

3.2.1. Catalyst screening. As depicted in Fig. 5a, the fructose dehydration to HMF catalyzed by Nb_2O_5 was conducted at 120 °C for 60 minutes. This was done to facilitate a comparison with the catalytic efficiency of $SrNb_2O_6$ catalysts, in which Sr species are incorporated into the structure of Nb oxides. It can be observed in the figure that an increase in reaction time led to a boost in fructose conversion and HMF yield accordingly. Its catalytic performance improved slowly during the first 30 minutes, but sharply at 60 min with the maximum fructose conversion and HMF yield reaching up to 89.0% and 68.5%,

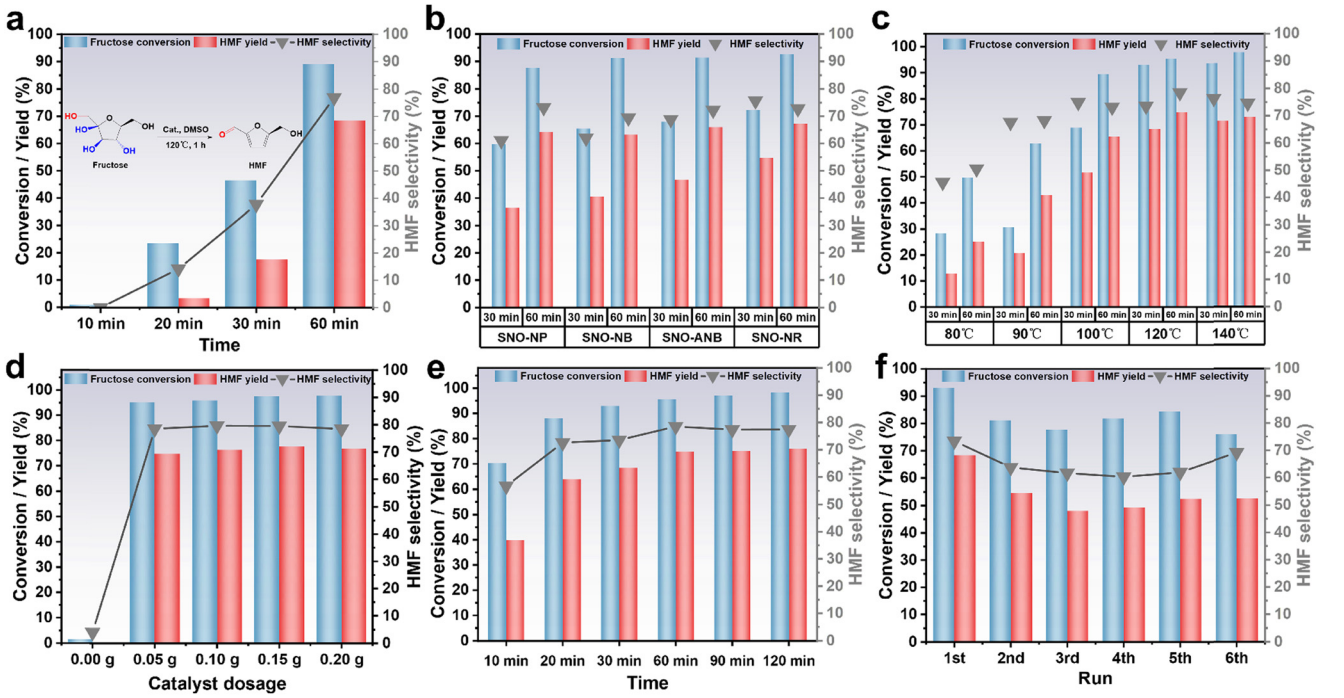

Fig. 5 Catalytic performance of various catalysts: (a) Nb_2O_5 and (b) SNO catalysts with various morphologies. Effects of (c) reaction temperature, (d) catalyst dosage, and (e) reaction time on the dehydration of fructose to HMF over SNO-NR. (f) Recycle tests over SNO-NR. Reaction conditions: 4 wt% fructose solution (5 mL DMSO), 120 °C, 60 min, 0.05 g catalyst except for (b) 110 °C, (c) 80–140 °C, (d) 0.00–0.20 g catalyst, (e) 10–120 min, and (f) 30 min.

respectively. Fig. 5b shows the comparison of catalytic performance toward fructose dehydration into HMF using $SrNb_2O_6$ catalysts with different morphologies at a reaction temperature of 110 °C for 30–60 min. Likewise, both fructose conversion and HMF yield increased gradually as the reaction time proceeded for all four SNO materials. The difference between their catalytic performance was more pronounced at 30 min, where the catalytic activity of SNO-NR was revealed as the highest with 72.3% fructose conversion and 54.7% HMF yield, while SNO-NP showed the minimum values of 59.7% and 36.5% respectively. This result may be primarily ascribed to more accessible active sites on the catalyst surface of SNO-NR and higher B/L ratio in the aforementioned discussion. A similar trend could be observed in the context of 60 min where each SNO catalyst exhibited approaching catalytic activity, yet the highest fructose transformation and HMF yield were still obtained by SNO-NR, reaching up to 92.6% and 67.3%, respectively. SNO-ANB came second with a conversion of 91.4% and yield of 66.0%. The distinct differences between the catalytic performance of these four SNO catalysts may be associated with various preparation conditions leading to differences in their intrinsic physicochemical properties such as crystal growth characteristics and acid properties as discussed in section 3.1. Therefore, the optimum catalyst was selected as SNO-NR for the subsequent investigation into the effects of different factors on the catalytic performance to optimize the reaction parameters.

3.2.2. Reaction parameter optimization. The effects of reaction temperature, catalyst dosage, and reaction time on the fructose dehydration to HMF over the SNO-NR catalyst were further investigated within the range of 80–140 °C, 0.00–0.20 g, and 10–120 min, respectively. It can be observed from Fig. 5c that fructose was consumed faster at higher temperatures. Overall, an increase in reaction temperature and time led to an increase of fructose conversion and HMF yield accordingly. For instance, the conversion rate and HMF yield increased progressively from 28.3% to 93.7% and from 12.9% to 71.5%, respectively, with temperature increasing from 80 to 140 °C at the reaction time of 30 min. Likewise, they increased gradually from 68.9% to 89.5% and from 51.6% to 65.5% at 100 °C as the reaction time proceeded. These results indicated that sufficient reaction time and high temperature facilitate the fructose catalytic conversion process. It is important to note that these values appeared to reach a plateau gradually and even decreased slightly at 140 °C at 60 min. This implied that overreaction resulting from higher temperatures and longer time under certain conditions would lead to the formation of undesirable by-products. A similar phenomenon could also be observed in the variation of HMF selectivity as reaction temperature varied. It initially demonstrated a rapid increase from 80 °C to 100 °C, followed by a plateau of slow rise and even slight decline as the temperature further increased to 140 °C. Therefore, the optimum HMF yield of 74.9% was obtained at 120 °C for 60 min with a high fructose conversion of 95.4%. Additionally, it is important to compare this result obtained by SNO-NR with those by Nb_2O_5 as illustrated in Fig. 5a from which the former catalyst exhibiting better catalytic effectiveness and faster reaction kinetics than the latter could be concluded. Further, the effect of catalyst dosage on catalytic efficacy was examined under these optimal conditions, as shown in Fig. 5d. For comparison, a fructose solution without any catalyst was also subjected to the same reaction conditions in order to validate the contribution of other factors to the overall catalytic performance. It was found that very limited HMF could be obtained from fructose under these conditions. The effective catalytic performance was observed as the catalyst dosage increased. Specifically, the fructose conversion rate continually increased to 95.4% and HMF yield increased to 74.9% with the addition of only 0.05 g catalyst. The highest HMF yield of 77.7% was achieved at the catalyst dosage of 0.15 g although it was not a significant improvement compared with the result of 0.05 g catalyst and could hardly be further enhanced by the continuous increase of catalyst dosage. A slight decrease in HMF yield was observed even, which could be ascribed to potentially excessive active sites resulting in undesired reactions. Given that varying catalyst dosage demonstrated approximate catalytic performance, the optimum catalyst addition was still 0.05 g due to potential environmental impact and cost efficiency. Additionally, Fig. 5e displays the effect of reaction time on the fructose-to-HMF dehydration reaction under these predetermined conditions. As observed in this figure, an extended reaction time from 10 min up to 120 min contributed to the unceasing increase of fructose conversion into HMF and final near-finished transformation. The highest HMF yield of 76.1% was obtained at the reaction time of 120 min which was close to that of 60 min. This indicates that the reaction was essentially completed within 60 minutes. In summary, the optimum HMF yield of 74.9% was obtained at 120 °C for 60 min with a high fructose conversion of 95.4% when 0.05 g catalyst was added.

3.2.3. Catalyst stability and reusability tests. The stability and reusability of the SNO-NR catalyst were further evaluated in 4 wt% fructose solution (5 mL DMSO) with a catalyst dosage of 50 mg at 120 °C for 30 min (Fig. 5f). Normal recycling measure involves centrifugation after reaction, washing twice with ethanol, and finally oven-drying at 60 °C for the next run. As seen from the figure, a decrease in the DFF yield from 68.4% achieved by the fresh SNO-NR to 54.6% by the reused one was observed under the same reaction conditions. Then this value further declined to 48.0% in the 3rd run, followed by a plateau and even slight resurgence till the 6th run of 52.5%. The initial activity loss may be mainly due to decreased acid capacity and imbalanced B/L ratio, as supported by the Py-IR analysis in section 3.1.2. Nevertheless, such negligible deactivation confirmed the robustness of SNO-NR, proved by ICP results where insignificant amounts of Sr (61–92 ppb) were detected in the leachate. This conclusion was in good alignment with diverse characterization analyses as discussed in section 3.1.

3.2.4. By-product analysis. The types of by-products were identified by combination of GC-MS and HPLC analytical techniques as revealed in Fig. S2 and S3 correspondingly. It was found in the figures that the dominant product was HMF, and the concentration of other by-products was excessively low. Specifically in Fig. S2, the most prominent peak at 13.08 min represented HMF, whereas the faint peaks at 7.16 min and 7.32 min, respectively, were mainly attributed to 2,5-furandicarboxaldehyde and furyl hydroxymethyl ketone, respectively. The negligible peak at 6.66 min might be related to impurities. As for Fig. S3, the most remarkable peak at 25.97 min was ascribed to the solvent peak, and the second noteworthy signal at 28.71 min revealed the presence of HMF. For the weak peaks eluted before 20 min, ~8–9 min signified the existence of glucose and fructose while the almost indistinguishable peak at around 15 min was associated with levulinic acid (LA). These results were obtained and determined by comparing them with standard samples. Collectively, several by-products involving glucose, levulinic acid, 2,5-furandicarboxaldehyde, and furyl hydroxymethyl ketone were recognized by HPLC and GC-MS analysis. They were generated through side reactions by the isomerization of fructose, the rehydration of HMF, the oxidation of HMF, and the condensation of HMF, respectively. Their extremely low contents indicated that the fructose dehydration reaction in DMSO over SNO-NR was selective for HMF generation and could effectively avoid these side reactions.

3.3. Plausible reaction mechanism

3.3.1. Pathway for HMF formation from fructose dehydration in DMSO. The pathway for the formation of HMF by dehydration of fructose was investigated by *in situ* ^{1}H NMR. Fig. 6a shows the time progression of the NMR spectra for fructose dehydration to HMF over SNO-NR in DMSO-d_6 at 120 °C. The peaks between 3.0 and 4.5 ppm were attributed to fructose while the peak at 3.3 ppm was assigned to H_2O in DMSO-d_6. Additionally, the peaks at 4.48, 6.58, 7.48, and 9.53 ppm were ascribed to HMF.[63] As the reaction time increased from 0 to 120 min (120 °C), the intensity of HMF peaks gradually enhanced whereas the fructose peaks faded. This result indicated that fructose reactants dehydrated progressively to form HMF products. No signals associated with other potential by-products, such as levulinic acid, were observed in the ^{1}H NMR spectra under these conditions. This might be due to its concentration being below the detection limit as supported by the discussion in the previous section. It could be suggested that this SNO-NR-catalyzed fructose-to-HMF conversion reaction was selective, which was in good accordance with the aforementioned conclusions.

3.3.2. Comparison of catalytic performance and possible reaction mechanism. The $SrNb_2O_6$-catalyzed dehydration of fructose into HMF in DMSO demonstrated a conspicuous catalytic performance among various heterogeneous metal-based catalysts as summarized in Table 4 with a high HMF yield of 74.9% and impressive selectivity of 78.5%. Such achievements could be largely credited to specific structural and physicochemical properties of the SNO-NR crystallites, especially the presence of sufficient acid capacity and optimal B/L ratio with their synergistic effects as previously discussed playing crucial roles in activating fructose transformation into highly selective HMF. It is also important to mention that DMSO as the reaction solvent possesses one of the benefits associated with water produced during the fructose dehydration reaction.[64] Specifically, side reactions that involve the rehydration of HMF due to the intermediate water, resulting in the formation of levulinic acid and formic acid, might be greatly suppressed when DMSO is sufficiently in excess to combine with all the water released during the reaction. This could also be another factor in the high selectivity for HMF formation in DMSO compared with other solvents in Table 4.[65,66] A possible mechanism for fructose dehydration to HMF over the SNO-NR catalyst is proposed in Fig. 6b. First, the reaction route shown in the figure involved initial adsorption of fructose molecules on the SNO-NR surface, where both B-acid sites and L-acid sites actively participated in the dehydration steps. On the one hand, B-acid sites facilitated the protonation of the hydroxyl groups in the fructose molecules. On the other hand, L-acid sites helped to stabilize

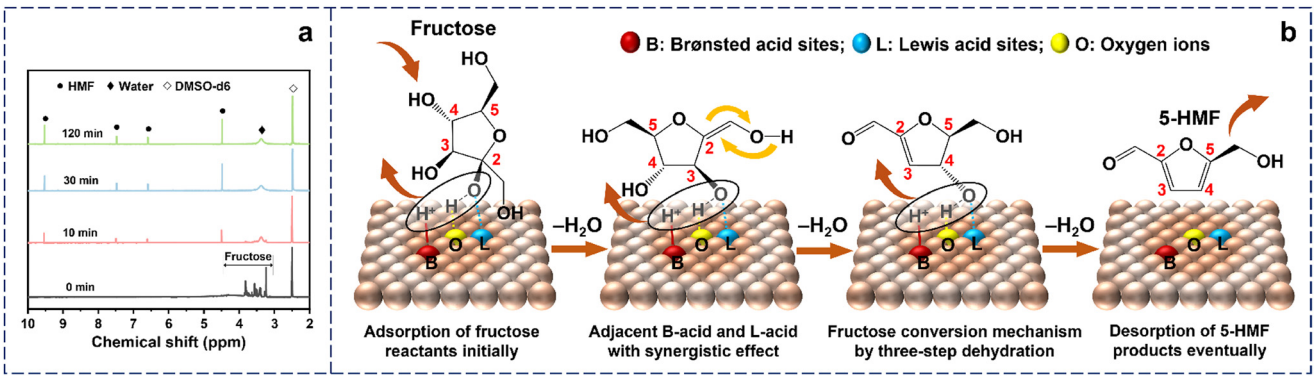

Fig. 6 (a) *In situ* ^{1}H NMR spectra as a function of time for the dehydration of 4 wt% fructose catalyzed by SNO-NR in DMSO-d_6 at 120 °C. (b) Proposed reaction mechanism for the SNO-catalyzed dehydration of fructose to HMF.

Table 4 Various heterogeneous catalysts for fructose dehydration to HMF

Catalyst	Solvent	Temp. (°C)	Time (min)	HMF yield (%)	Reference
Mesoporous TiO_2	Water	120	5	32.8	9
Sulfonated carbon	Water	120	960	35.6	71
$Nb_2O_5{\cdot}nH_2O$	2-Butanol/H_2O-5 : 2, V/V	140	120	42.0	72
S-GCN	Water	200	300	43.0	73
Sulfonated lignin carbon	DMSO	130	40	50.8	74
SO_4/WO_x–ZrO_2	DMSO	140	5	70.8	75
SO_4^{2-}/ZrO_2	Acetone–DMSO	180	20	72.8	76
SBA-15-SO_3H	Ionic liquid	120	60	81.0	21
M-ZrO_2/SO_4^{2-}	DMSO	120	60	85.0	77
$SrNb_2O_6$-NR	DMSO	120	60	74.9	This work

the transition state of the dehydration reaction. This coordination may enhance the electrophilicity of carbonyl carbon, making it more susceptible to nucleophilic attack by the B-acid which was conducive to the elimination of water to form HMF as reported in ref. 51, 67 and 68. Then, under the synergistic effect of B-acid and L-acid sites on this bifunctional catalyst surface, the C_2–OH of the reactant fructose was attacked by the H^+ provided by the B-acid sites on SNO-NR to complete the first dehydration step. After that, the C=C bond on the ring was attacked to form the –CHO group and the second water molecule was lost. Further, the C_4–OH bond on the ring was also attacked by the protonation effect and the third water molecule was lost. After the three-step dehydration catalyzed by the adjacent B-acid and L-acid sites on SNO-NR, the final product 5-HMF was formed and released eventually from the catalyst surface.[55,69,70]

4. Conclusions

This study introduced bifunctional $SrNb_2O_6$ catalysts for the efficient dehydration of fructose into HMF. The catalysts differed in pH values as well as niobium additions during the synthesis process and were successfully prepared using a facile one-step hydrothermal method. Screening of $SrNb_2O_6$ with various morphologies revealed the best performance of SNO-NR with a yield of 74.9% and selectivity of 78.5% under optimized reaction conditions within 1 h at 120 °C in DMSO. This could be credited to its superiority in physicochemical properties, especially sufficient acid capacity and balanced B/L acid ratio with synergistic effects, which were verified by diverse characterization analyses. Furthermore, this SNO-NR catalyst could be reused successively for six runs without substantial loss in activity. Overall, the development of $SrNb_2O_6$ catalysts in this work not only advances the design of Nb-based metal catalysts but also provides valuable insights into the potential application of these materials as recyclable catalysts in sustainable biorefineries, promoting more efficient and eco-friendly conversion processes. Given the limitations associated with fructose as a feedstock, future research will focus on extending this catalytic system to more abundant and cost-effective substrates such as glucose and cellulose, with the aim of further enhancing the practical applicability and sustainability of HMF production.

Conflicts of interest

The authors declare no competing interest.

Data availability

The data supporting this article have been included as part of the SI.

Supplementary information is available: containing additional experimental details (Py-FTIR and NMR), characterization data (porosity, GC-MS, and HPLC analysis), and corresponding figures. See DOI: **https://doi.org/10.1039/D5CY00613A**.

Acknowledgements

The work described in this paper was partially supported by a grant from the Research Grants Council of the Hong Kong Special Administrative Region, China (Project No. HKBU 12202723) and Environment and Conservation Fund (127/2022).

References

1 J. Huang, J. Wang, Z. Huang, T. Liu and H. Li, Photothermal technique-enabled ambient production of microalgae biodiesel: Mechanism and life cycle assessment, *Bioresour. Technol.*, 2023, **369**, 128390.
2 S. G. W. Huber, S. Iborra and A. Corma, Synthesis of Transportation Fuels from Biomass: Chemistry, Catalysts, and Engineering, *Chem. Rev.*, 2006, **106**, 4044–4098.
3 J. J. Bozell, Chemistry. Connecting biomass and petroleum processing with a chemical bridge, *Science*, 2010, **329**, 522–523.
4 H. Zhao, J. E. Holladay, H. Brown and Z. C. Zhang, Metal chlorides in ionic liquid solvents convert sugars to 5-hydroxymethylfurfural, *Science*, 2007, **316**, 1597–1600.
5 A. A. Rosatella, S. P. Simeonov, R. F. M. Frade and C. A. M. Afonso, 5-Hydroxymethylfurfural (HMF) as a building block platform: Biological properties, synthesis and synthetic applications, *Green Chem.*, 2011, **13**, 754–793.
6 L. Zhou, R. Liang, Z. Ma, T. Wu and Y. Wu, Conversion of cellulose to HMF in ionic liquid catalyzed by bifunctional ionic liquids, *Bioresour. Technol.*, 2013, **129**, 450–455.

7 X. Liu, Y. Luo, H. Ma, S. Zhang, P. Che, M. Zhang, J. Gao and J. Xu, Hydrogen-Binding-Initiated Activation of O-H Bonds on a Nitrogen-Doped Surface for the Catalytic Oxidation of Biomass Hydroxyl Compounds, *Angew. Chem., Int. Ed.*, 2021, **60**, 18103–18110.
8 S. Umasankar and P. Tamizhdurai, Effect of copper on NiCu bimetallic catalyst supported on SBA-16 for the catalytic hydrogenation of 5-hydroxymethylfurfural to 2,5-dimethylfuran, *Biomass Bioenergy*, 2020, **143**, 105868.
9 S. Dutta, S. De and B. Saha, A Brief Summary of the Synthesis of Polyester Building-Block Chemicals and Biofuels from 5-Hydroxymethylfurfural, *ChemPlusChem*, 2012, **77**, 259–272.
10 M. J. Climent, A. Corma and S. Iborra, Conversion of biomass platform molecules into fuel additives and liquid hydrocarbon fuels, *Green Chem.*, 2014, **16**, 516–547.
11 T. Deng, X. Cui, Y. Qi, Y. Wang, X. Hou and Y. Zhu, Conversion of carbohydrates into 5-hydroxymethylfurfural catalyzed by $ZnCl_2$ in water, *Chem. Commun.*, 2012, **48**, 5494–5496.
12 Y. Zhao, K. Lu, H. Xu, L. Zhu and S. Wang, A critical review of recent advances in the production of furfural and 5-hydroxymethylfurfural from lignocellulosic biomass through homogeneous catalytic hydrothermal conversion, *Renewable Sustainable Energy Rev.*, 2021, **139**, 110706.
13 Q. Ren, H. Ma, W. Wang, C. Chen, J. Xiao and P. Che, Catalytic dehydration of fructose to 5-hydroxymethylfurfural over mesoporous Nb-W oxide solid acid catalyst, *Biomass Bioenergy*, 2023, **174**, 106860.
14 C. Thoma, J. Konnerth, W. Sailer-Kronlachner, P. Solt, T. Rosenau and H. W. G. van Herwijnen, Current Situation of the Challenging Scale-Up Development of Hydroxymethylfurfural Production, *ChemSusChem*, 2020, **13**, 3544–3564.
15 Z. Hosseini, M. Kazemeini, S. Sadjadi and S. Pourebrahimi, Silicotungstic acid catalyst supported onto functionalized halloysite nanotubes (HNTs) utilized for the production of 5-hydroxymethylfurfural (5-HMF) from fructose, *Mol. Catal.*, 2024, **557**, 113992.
16 K. L. G. L. Rorrer, Reaction Rates for the Partial Dehydration of Glucose to Organic Acids in Solid-Acid, Molecular-Sieving Catalyst Powders, *J. Chem. Technol. Biotechnol.*, 1997, **69**, 35–44.
17 Y. Li, X. Lu, L. Yuan and X. Liu, Fructose decomposition kinetics in organic acids-enriched high temperature liquid water, *Biomass Bioenergy*, 2009, **33**, 1182–1187.
18 G. Yong, Y. Zhang and J. Y. Ying, Efficient catalytic system for the selective production of 5-hydroxymethylfurfural from glucose and fructose, *Angew. Chem., Int. Ed.*, 2008, **47**, 9345–9348.
19 F. Wang, H. Z. Wu, C. L. Liu, R. Z. Yang and W. S. Dong, Catalytic dehydration of fructose to 5-hydroxymethylfurfural over Nb_2O_5 catalyst in organic solvent, *Carbohydr. Res.*, 2013, **368**, 78–83.
20 T. Okuhara, Water-Tolerant Solid Acid Catalysts, *Chem. Rev.*, 2002, **102**, 3641–3666.
21 X. Guo, Q. Cao, Y. Jiang, J. Guan, X. Wang and X. Mu, Selective dehydration of fructose to 5-hydroxymethylfurfural catalyzed by mesoporous SBA-15-SO(3)H in ionic liquid BmimCl, *Carbohydr. Res.*, 2012, **351**, 35–41.
22 V. V. Ordomsky, J. van der Schaaf, J. C. Schouten and T. A. Nijhuis, The effect of solvent addition on fructose dehydration to 5-hydroxymethylfurfural in biphasic system over zeolites, *J. Catal.*, 2012, **287**, 68–75.
23 N. C. IzabelaNowakandMariaZiolek, Preparation, Characterization, and Application in Heterogeneous Catalysis, *Chem. Rev.*, 1999, **99**, 3603–3624.
24 K. Tanabe and S. Okazaki, Various reactions catalyzed by niobium compounds and materials, *Appl. Catal., A*, 1995, **133**, 191–218.
25 K. Tanabe, Catalytic application of niobium compounds, *Catal. Today*, 2003, **78**, 65–77.
26 F. Yang, Q. Liu, X. Bai and Y. Du, Conversion of biomass into 5-hydroxymethylfurfural using solid acid catalyst, *Bioresour. Technol.*, 2011, **102**, 3424–3429.
27 M. Kim, Y. Su, A. Fukuoka, E. J. M. Hensen and K. Nakajima, Aerobic Oxidation of 5-(Hydroxymethyl)furfural Cyclic Acetal Enables Selective Furan-2,5-dicarboxylic Acid Formation with CeO(2) -Supported Gold Catalyst, *Angew. Chem., Int. Ed.*, 2018, **57**, 8235–8239.
28 D. Stošić, S. Bennici, V. Pavlović, V. Rakić and A. Auroux, Tuning the acidity of niobia: Characterization and catalytic activity of Nb_2O_5–MeO_2 (Me = Ti, Zr, Ce) mesoporous mixed oxides, *Mater. Chem. Phys.*, 2014, **146**, 337–345.
29 J. Guo, S. Zhu, Y. Cen, Z. Qin, J. Wang and W. Fan, Ordered mesoporous Nb–W oxides for the conversion of glucose to fructose, mannose and 5-hydroxymethylfurfural, *Appl. Catal., A*, 2017, **200**, 611–619.
30 S. Mahala, Senthil Murugan Arumugam, Ravi Kumar Kunchala, Bhawana Devi, and Sasikumar Elumalai, Mesoporous Ta_2O_5/Nb_2O_5 nanocomposite with Lewis/Brønsted acid sites to enhance stepwise glucose conversion to 5-hydroxymethylfurfural, Sustainable, *Energy Fuels*, 2024, **8**, 2219–2234.
31 E. I. Garcia-Lopez, F. R. Pomilla, B. Megna, M. L. Testa, L. F. Liotta and G. Marci, Catalytic Dehydration of Fructose to 5-Hydroxymethylfurfural in Aqueous Medium over Nb(2) O(5)-Based Catalysts, *Nanomaterials*, 2021, **11**, 1821.
32 I. S. Cho, S. Lee, J. H. Noh, D. W. Kim, D. K. Lee, H. S. Jung, D. W. Kim and K. S. Hong, $SrNb_2O_6$ nanotubes with enhanced photocatalytic activity, *J. Mater. Chem.*, 2010, **20**, 3979–3983.
33 X. L. Tao Huang, J. Xing, F. H. Wendeng Wang and Z. Shan, Photocatalytic activities of hetero-junction semiconductors WO_3/$SrNb_2O_6$, *Mater. Sci. Eng., B*, 2007, **141**, 49–54.
34 S. Xie, Y. Wang, Q. Zhang, W. Deng and Y. Wang, $SrNb_2O_6$ nanoplates as efficient photocatalysts for the preferential reduction of CO_2 in the presence of H_2O, *Chem. Commun.*, 2015, **51**, 3430–3433.
35 R. Pang, K. Teramura, H. Asakura, S. Hosokawa and T. Tanaka, Highly selective photocatalytic conversion of CO_2 by water over Ag-loaded $SrNb_2O_6$ nanorods, *Appl. Catal., B*, 2017, **218**, 770–778.

36 N. Abid, A. M. Khan, S. Shujait, K. Chaudhary, M. Ikram, M. Imran, J. Haider, M. Khan, Q. Khan and M. Maqbool, Synthesis of nanomaterials using various top-down and bottom-up approaches, influencing factors, advantages, and disadvantages: A review, *Adv. Colloid Interface Sci.*, 2022, **300**, 102597.

37 S. Liang, L. Wu, J. Bi, W. Wang, J. Gao, Z. Li and X. Fu, A novel solution-phase approach to nanocrystalline niobates: selective syntheses of $Sr_{0.4}H_{1.2}Nb_2O_6.H_2O$ nanopolyhedrons and $SrNb_2O_6$ nanorods photocatalysts, *Chem. Commun.*, 2010, **46**, 1446–1448.

38 D. C. J. Ye, Selective-Synthesis of High Performance Single-Crystalline Sr2Nb2O7 Nanoribbon and SrNb2O6 Nanorod Photocatalysts, *Chem. Mater.*, 2009, **21**, 2327–2333.

39 G. F. Harrington and J. Santiso, Back-to-Basics tutorial: X-ray diffraction of thin films, *J. Electroceram.*, 2021, **47**, 141–163.

40 R. Kužel, J. Čížek and M. Novotný, On X-Ray Diffraction Study of Microstructure of ZnO Thin Nanocrystalline Films with Strong Preferred Grain Orientation, *Metall. Mater. Trans. A*, 2012, **44**, 45–57.

41 A. Pandey, S. Dalal, S. Dutta and A. Dixit, Structural characterization of polycrystalline thin films by X-ray diffraction techniques, *J. Mater. Sci.: Mater. Electron.*, 2021, **32**, 1341–1368.

42 Q. Ye, C. Liu, P. Wu, J. Wu, L. Lin, Y. Li, Z. Ahmed, S. Rehman and N. Zhu, Insights into photocatalytic degradation of phthalate esters over MSnO(3) perovskites (M = Mg, Ca): Experiments and density functional theory, *J. Environ. Manage.*, 2022, **307**, 114511.

43 Y. Li, J. Zhao and B. Wang, Low temperature preparation of nanocrystalline $Sr_{0.5}Ba_{0.5}Nb_2O_6$ powders using an aqueous organic gel route, *Mater. Res. Bull.*, 2004, **39**, 365–374.

44 Q. Liu, Q. Zhang, B. Liu and W. L. Dai, Facile one-step hydrothermal synthesis of single-crystalline $SnNb_2O_6$ nanosheets with greatly extended visible-light response for enhanced photocatalytic performance and mechanism insight, *Nanotechnology*, 2020, **32**, 065705.

45 H. T. Kreissl, M. M. J. Li, Y. K. Peng, K. Nakagawa, T. J. N. Hooper, J. V. Hanna, A. Shepherd, T. S. Wu, Y. L. Soo and S. C. E. Tsang, Structural Studies of Bulk to Nanosize Niobium Oxides with Correlation to Their Acidity, *J. Am. Chem. Soc.*, 2017, **139**, 12670–12680.

46 M. A. A. Andrew, T. Y. Wolek, H. N. Pham, S. Alayoglu, K. Abhaya and J. M. N. Datye, Creating Brønsted Acidity at the SiO_2-Nb_2O_5 Interface, *J. Catal.*, 2021, **394**, 387–396.

47 J. Liu, X. Cheng, X. Qi, N. Li, J. Tian, B. Qiu, K. Xu and D. Qu, Recovery of phosphate from aqueous solutions via vivianite crystallization: Thermodynamics and influence of pH, *Chem. Eng. J.*, 2018, **349**, 37–46.

48 H. Cheng, N. Yang, Q. Lu, Z. Zhang and H. Zhang, Syntheses and Properties of Metal Nanomaterials with Novel Crystal Phases, *Adv. Mater.*, 2018, **30**, e1707189.

49 A. Y. Lee, D. Erdemir and A. S. Myerson, Crystals and Crystal Growth, in *Handbook of Industrial Crystallization*, 2019, vol. 3, pp. 32–75.

50 C. Yan, S. Zheng, N. Chen, S. Yuan, Y. Chen, B. Li and Y. Zhang, Sulfated zirconia catalysts supported on mesoporous Mg-SBA-15 with different morphologies for highly efficient conversion of fructose to 5-hydroxymethylfurfural, *Microporous Mesoporous Mater.*, 2021, **328**, 111507.

51 E. Tututi-Ríos, H. González, A. Gutiérrez-Alejandre and J. L. Rico, Conversion of fructose over mesoporous Sn-KIT-6-$PrSO_3H$ catalysts: Impact of the Brønsted/Lewis acid sites molar ratio on the main reaction pathways, *Microporous Mesoporous Mater.*, 2024, **370**, 113051.

52 M. Li, L. Huai, Y. Zhang, H. Ma, P. Zhang, F. Xu, J. Zhang and L. Jiang, A binary catalytic system of sulfonated metal–organic frameworks and deep eutectic solvents towards highly efficient synthesis of 5-hydroxymethylfurfural from fructose, *Chem. Eng. J.*, 2024, **493**, 152767.

53 V. Choudhary, S. H. Mushrif, C. Ho, A. Anderko, V. Nikolakis, N. S. Marinkovic, A. I. Frenkel, S. I. Sandler and D. G. Vlachos, Insights into the interplay of Lewis and Bronsted acid catalysts in glucose and fructose conversion to 5-(hydroxymethyl)furfural and levulinic acid in aqueous media, *J. Am. Chem. Soc.*, 2013, **135**, 3997–4006.

54 V. Choudhary, S. I. Sandler and D. G. Vlachos, Conversion of Xylose to Furfural Using Lewis and Brønsted Acid Catalysts in Aqueous Media, *ACS Catal.*, 2012, **2**, 2022–2028.

55 X. Zhang, H. Lu, K. Wu, Y. Liu, J. Wu, Y. Zhu and B. Liang, Synergistic activation of hydroxyl groups by hierarchical acid sites and deep eutectic solvents for the dehydration of fructose to 5-hydroxymethylfurfural under mild temperature, *Renewable Energy*, 2024, **233**, 121144.

56 K. Saravanan, K. S. Park, S. Jeon and J. W. Bae, Aqueous Phase Synthesis of 5-Hydroxymethylfurfural from Glucose over Large Pore Mesoporous Zirconium Phosphates: Effect of Calcination Temperature, *ACS Omega*, 2018, **3**, 808–820.

57 Y. Zhong, Y. Liu, S. Wang, S. Hou and Y. Fan, Incorporation of tin oxide nanoparticles on sulfonated carbon microspheres as a bifunctional catalyst for efficient conversion of biomass-derived monosaccharides to 5-Hydroxymethylfurfural and furfural, *Ind. Crops Prod.*, 2024, **208**, 117913.

58 Y. Zheng, Y. Yang, Y. Zhang, W. Zou, Y. Luo, L. Dong and B. Gao, Facile one-step synthesis of graphitic carbon nitride-modified biochar for the removal of reactive red 120 through adsorption and photocatalytic degradation, *BioChar*, 2019, **1**, 89–96.

59 S. S. K. Fukushima, XPS Analysis on Nb-$SrTiO_3$ Thin Films Deposited with Pulsed Laser Ablation Technique, *J. Eur. Ceram. Soc.*, 1999, **19**, 1423–1426.

60 V. Young and T. Otagawa, XPS studies on strontium compounds, *Appl. Surf. Sci.*, 1985, **20**, 228–248.

61 N. Ozer, T. Barreto and C. M. L. Temel Biiyiiklimanli, Characterization of sol-gel deposited niobium pentoxide films for electrochromic devices, *Sol. Energy Mater. Sol. Cells*, 1995, **36**, 433–443.

62 L. Kong, C. Zhang, J. Wang, W. Qiao, L. Ling and D. Long, Nanoarchitectured Nb_2O_5 hollow, Nb_2O_5@carbon and NbO_2@carbon Core-Shell Microspheres for Ultrahigh-Rate Intercalation Pseudocapacitors, *Sci. Rep.*, 2016, **6**, 21177.

63 F. Jiang, Q. Zhu, D. Ma, X. Liu and X. Han, Direct conversion and NMR observation of cellulose to glucose and

5-hydroxymethylfurfural (HMF) catalyzed by the acidic ionic liquids, *J. Mol. Catal. A: Chem.*, 2011, **334**, 8–12.

64 R. M. Musau and R. M. Munavu, The Preparation of 5-Hydroxymethyi-2-Furaldehyde (HMF) from D-Fructose in the Presence of DMSO, *Biomass*, 1987, **13**, 67–74.

65 X. Qi, M. Watanabe, T. M. Aida and J. R. L. Smith, Catalytic dehydration of fructose into 5-hydroxymethylfurfural by ion-exchange resin in mixed-aqueous system by microwave heating, *Green Chem.*, 2008, **10**, 799–805.

66 F. Wang, A. W. Shi, X. X. Qin, C. L. Liu and W. S. Dong, Dehydration of fructose to 5-hydroxymethylfurfural by rare earth metal trifluoromethanesulfonates in organic solvents, *Carbohydr. Res.*, 2011, **346**, 982–985.

67 L. R. Domingo, M. Rios-Gutierrez and P. Perez, Understanding the Electronic Effects of Lewis Acid Catalysts in Accelerating Polar Diels-Alder Reactions, *J. Org. Chem.*, 2024, **89**, 12349–12359.

68 K. A. Resende, R. Zhao, Y. Liu, E. Barath and J. A. Lercher, Impact of Sn Lewis Acid Sites on the Dehydration of Cyclohexanol, *ACS Catal.*, 2024, **14**, 11741–11748.

69 P. Bhanja, A. Modak, S. Chatterjee and A. Bhaumik, Bifunctionalized Mesoporous SBA-15: A New Heterogeneous Catalyst for the Facile Synthesis of 5-Hydroxymethylfurfural, *ACS Sustainable Chem. Eng.*, 2017, **5**, 2763–2773.

70 X. Yang, M. M. Sadughi, A. Bahadoran, M. Al-Haideri, P. Ghamari Kargar, A. S. Noori and S. M. Sajjadinezhad, A new method for conversion of fructose and glucose to 5-hydroxymethylfurfural by magnetic mesoporous of SBA-16 was modified to sulfonic acid as Lewis's acid catalysts, *Renewable Energy*, 2023, **209**, 145–156.

71 A. Villa, M. Schiavoni, P. F. Fulvio, S. M. Mahurin, S. Dai, R. T. Mayes, G. M. Veith and L. Prati, Phosphorylated mesoporous carbon as effective catalyst for the selective fructose dehydration to HMF, Journal of Energy, *Chemistry*, 2013, **22**, 305–311.

72 G. F. T. B. Guo, L. Zhang, B. Yue, S. E. Tsang and H. Y. He, Effect of Brønsted/Lewis acid ratio on conversion of sugars to 5-hydroxymethylfurfural over mesoporous Nb and Nb-W oxides, *Chin. J. Chem.*, 2017, **35**, 1529–1539.

73 T. Chhabra, A. Bahuguna, S. S. Dhankhar, C. M. Nagaraja and V. Krishnan, Sulfonated graphitic carbon nitride as a highly selective and efficient heterogeneous catalyst for the conversion of biomass-derived saccharides to 5-hydroxymethylfurfural in green solvents, *Green Chem.*, 2019, **21**, 6012–6026.

74 L. Hu, X. Tang, Z. Wu, L. Lin, J. Xu, N. Xu and B. Dai, Magnetic lignin-derived carbonaceous catalyst for the dehydration of fructose into 5-hydroxymethylfurfural in dimethylsulfoxide, *Chem. Eng. J.*, 2015, **263**, 299–308.

75 J. Wang, T. Qu, M. Liang and Z. Zhao, Microwave assisted rapid conversion of fructose into 5-HMF over solid acid catalysts, *RSC Adv.*, 2015, **5**, 106053–106060.

76 P. Wataniyakul, P. Boonnoun, A. T. Quitain, T. Kida, N. Laosiripojana and A. Shotipruk, Preparation of hydrothermal carbon acid catalyst from defatted rice bran, *Ind. Crops Prod.*, 2018, **117**, 286–294.

77 Y. Zhou, L. Zhang and S. Tao, Mesoporous ZrO_2 Nanopowder Catalysts for the Synthesis of 5-Hydroxymethylfurfural, *ACS Appl. Nano Mater.*, 2019, **2**, 5125–5131.